

Radial symmetries based decomposition of cell clusters in binary and gray level images

Oliver Schmitt^{a,*}, Maria Hasse^b

^a*Institute of Anatomy, University of Rostock, Gertrudenstr. 9, D-18055 Rostock, Germany*

^b*Institute of Mathematics, University of Rostock, Universitätsplatz 1, D-18051 Rostock, Germany*

Received 23 January 2007; received in revised form 3 October 2007; accepted 5 November 2007

Abstract

The segmentation of structures of complex cytological and histological images is a necessary intermediate step for image analysis that give rise to binary images. In many cases these binary images can be rather far away from a subsequent object specific quantification because biological structures digitized by optoelectronic devices may be situated close together so that they appear as one fused object in the projective image. Such fusions of objects may become complex so that large clusters of biological structures emerge. To quantify individual objects of a cluster they must be separated. The shape, size and intensity variation of cells in complex organs like the brain may breed planar configurations that can be splitted only inadequately by common techniques, e.g., watershed separation or basic morphological processing of images.

Considering iteratively object contours suitable features of saliency can be accumulated that give rise to markers of singular objects. Such significant markers may drive a separation process more effective than common approaches. The determination of markers by an iterative method should be scale, translation and rotation invariant and robust with regard to noise due to the variability of biological specimen.

We realize a technique that splits cell clumps consisting of different cell sizes and shapes into meaningful parts. The multiscale method applied here is based on the analysis of the contour shape and the object area by iterative voting using oriented kernels. These cone-shaped kernels vote iteratively for the local center of mass of the components of an aggregation. The voting is performed along the gradient of the distance transformation of the binarized image of aggregates. Iterative voting is initialized by voting along the gradient direction where at each iteration the voting direction and shape of the kernel is refined, resp. the kernel topography is refined and reoriented iteratively. It turned out that the kernel topography is unique because it votes for the most likely set of grid points where the gravity center of an individual cluster component may be located. Furthermore, a new procedure is realized to use the local intensities of aggregations for kernel voting. The last voted iteration provides gravitation centers, resp. centers of mass of the clumped cells. These are extracted and used as markers to determine individual cell boundaries by a marker based watershed postprocessing.

The subject of this paper is to highlight the basic algorithm of iterative kernel voting and expanding it to process intensities within clusters as well as contour information. The approach is applied to synthetic images that were modified systematically with regard to object topology. Natural aggregates of cells at the light microscopic level and cell clusters derived from high resolution flat bed scanning were splitted. In addition to these examples images from a benchmark databases were investigated. The splittings generated by the iterative voting approach were compared with expected splittings of test persons and with results of the watershed method. Especially the gray level based iterative voting method provides superior results for cell cluster separation in comparison to the watershed procedure.

© 2007 Elsevier Ltd. All rights reserved.

Keywords: Image analysis; Radial symmetry; Saliency; Points of interest; Center of mass; Iterative voting; Decomposition; Separation; Subdivision; Splitting; Partitioning; Cell cluster

1. Introduction

Digital cell measurements in diascopic micrographs of stained cells in histological sections are complex. Complexities arise as a result of nonuniform staining, local cell distributions

* Corresponding author. Tel.: +49 381 494 8408; fax: +49 381 494 8402.

E-mail addresses: schmitt@med.uni-rostock.de (O. Schmitt),
maria.hasse@uni-rostock.de (M. Hasse).

with different degrees of overlap and variability of their size and shape [1]. The section thickness leads to considerable differences of gray level or color distributions within cells. Thicker sections of 10 to 20 μm give rise to almost dark stained neurons whereby thin sections of about 5 μm yields a pale nucleus, a dark nucleolus and perikaryon. Many areas within the brain of vertebrates exhibit dense neuron distributions which even persist in thin sections where partial or total overlaps of structures in consequence of optical projection appear. Likewise optical fusion appears if cells are juxtaposed very closely like the small granular cells of the cerebellum or those in the dentate gyrus.

In summary, micrographs of stained histological sections of the brain contain with a high probability [2] overlaps of structures due to their distribution and projection of a 3D physical structure to a 2D-image.

These overlaps are reduced in confocal laser scanning microscopy (CLSM) [3,4]. However, for long term measurements of large areas of histological sections, for instance serial sections of brains, CLSM is inapplicable and motorized video microscopy [5] or high resolution transparent flat bed scanning [6] need to be performed.

Cytological as well as histological analysis of cell parameters [7–12] assume that the objects, i.e. cell bodies and/or cell nuclei, to be measured are not connected. Particularly reliable automatic processing of cytological and histological digital images is demanded for clinical routine purposes as well as for basic science. Naive methods like conditioned and scale space based erosion [13] result in an unsatisfying splitting if objects are juxtaposed very closely. Even, sophisticated procedures like watershed segmentation of heavily clustered cells with different shape and size may fail [14–24].

1.1. Review of previous work

Since many years [25–33] much effort has been spent to decompose such overlaps of cells because successful and robust splitting is the key for automation [34]. However, complex overlaps of hundreds or thousands of structures in images where the area of the foreground is larger than the background (Fig. 9g) the decomposition problem becomes complex. Automatic morphometry [35] of complex cell distributions in histological sections of biologic material becomes a challenging task in combination with registration of serial sections [36] because complete cell atlases of organs especially brains can be generated.

The problem of touching objects is propagated by image analytic processes followed by global segmentation done by standard methods [37–42] that produce bilevel images that contain sufficient foreground information for further cell-object specific processing.

The structural analysis of cytological images is performed often by means of morphological filters [43–46] because of their shape- rather than frequency-oriented operations [47]. Such nonlinear approaches are well suited for shape description [48] and decomposition [49,50]. The concept of morphological operations have been extended to multiscale shape

representations by Salembier and Kunt [51] and Goutsias and Heijmans [52]. Applying multiscale morphological processing (MMP) [53] an image containing fused regions that have to be partitioned is decomposed into size-specific scales, each carrying markers representing disjoint regions. The detected markers are used to reconstruct successively original shapes without fusing them again. This kind of morphology based separation can be adapted to different shapes of aggregated particles as shown by Talbot and Appleton [54] and Metzler et al. [46]. Aggregates that consists of particles of certain sizes can be segmented by morphological approaches although the shape and size of cells in biological specimens may vary considerably.

Aggregates may appear as two touching cells or large clusters with many holes, i.e., connected regions of background within an aggregate. For such complex clusters contour based algorithms are used. Mostly, these algorithms determine centroids of decomposed particles which are used thereafter for a precise gray scale based segmentation by the watershed method or region growing. Contour based algorithms determine dominant points, i.e., concavities and convexities of the contour and test which cut path or split path of opposite dominant points turns out to minimize a cost function. Further methods aim to separate aggregates by applying active contours and level sets. A comprehensive overview of recent literature concerning these families of aggregate-particle-problems and algorithms is given below:

- *Morphology based procedures* [14,18,19,55–59];
- *contour based techniques* [54,60–69];
- *active contour based methods* [35,70,71];
- *graph theoretic approaches* [72,73];
- *parametric fitting algorithms* [54,74–76] and
- *level set approach* [74,77].

1.2. Voting radial symmetries on clustered contours

For the recognition of single cells of a cell cluster the salient attributes are symmetry, continuity, and closure. Saliency is a central perceptual cue that occurs at different resolutions. Additionally, to the projective problems (incomplete information) mentioned above detection of these attributes is often hindered by noise and artifacts. Among these attributes, it is well known that symmetry is a preattentive process [78] that facilitates recognition, scene representation, reconstruction and separation of disjoint entities. Bilateral symmetry is given if the object is invariant under a reflection of a line (axis of symmetry) passing through the centroid of the object. An object is said to possess rotational symmetry of order n if it is invariant under rotations of $2\pi/n$ radians about its *center of mass*, whereby central symmetry is a special case of rotational symmetry with $n = 2$. An object is said to possess radial symmetry if it has bilateral and rotational symmetry (Fig. 1). Most symmetries of cells in the central nervous system are not perfect symmetries. Therefore, we are using radial symmetries not in terms of strict symmetries rather than allow deviations from the ideal. The *center of mass* in biological cells is considered as a basic perceptual event that supports separation of clustered cells.

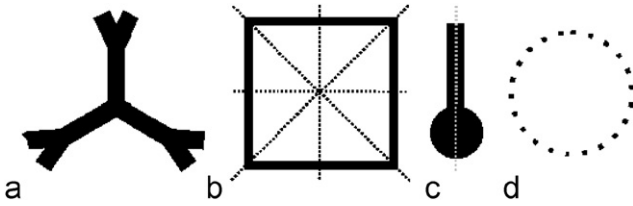


Fig. 1. Examples of different types of symmetries. (a) Rotational symmetry of order 3, (b) quadrilateral symmetries with dashed lines as axes, (c) bilateral symmetry, and (d) radial symmetry.

The complexities mentioned above are addressed through a special class of iterative voting, which is kernel-based, and its topography favors radial symmetries. It is robust with respect to variation in size and intensity, and delineates overlapped compartments. Using the concept of radial symmetries inference of the center of mass from incomplete boundaries of single cells as they occur in profiles of overlapping cells is realized by voting an evolving kernel. Perceptual grouping performed through the refinement of spatially tuned voting kernels leads to information of disjoint events.

Radial symmetries represent a superset of circular symmetries whereby the bulk of previous research has been limited to the latter class [79–83]. The techniques in circular symmetries are

- point operations leading to intensity outputs,
- clustering based on parametrized shape model or voting and
- iterative techniques.

The point operations use image gradients and orientations to infer the center of mass [84–86]. Spatial voting and the concept of summing certain parameters in an accumulator space has been studied at least four decades [63]. Hough introduced the notion of parametric clustering in terms of well-defined geometry of objects which possess regular shapes (circles or ellipses) [87] which was later extended to the generalized Hough transform. These techniques produce points of convergence corresponding to the parametric models of well-known geometries. These distributions are merged and model parameters are refined. The nonparametric clustering techniques operate along the direction of gradients to search for line- or area-based radial symmetry. The line-based search is known as spoke filter. The frequency of occurrence of points normal to the edge direction are accumulated. The area-based voting cluster votes in a small neighborhood along the gradient direction. The watershed transform is one example and a further the regularized centroid transform (RCT) which iteratively transport boundary points to the local centers of mass [88–90]. To obtain robust results with regard to noise the RCT regularizes the solution to the centroid transform to eliminate inherent singularities.

Principally, voting operates on the notion of continuity and proximity at different scales, e.g., points, lines, convex objects. Yang and Parvin [91] have demonstrated that a series of kernels that vote iteratively for the likelihood of the center of mass exhibit disjoint centers of masses in images containing cell

clusters. Generally, this approach is comprised by the curve evolution techniques [92]. Iterative voting turns out to retain sufficient noise immunity which is important with regard to noisy microscopic cell images. The iterative approach refines the center of mass at each iteration until it converges to a focal response. The applied kernels are cone-shaped and controlled by parameters to target geometric features. The voting kernels are applied within the gradient direction. At each iteration and location on the contour the voting kernel is aligned along the maximum response of the voting space. Additionally, the shape of the kernel is refined and focused within the iterative process. We extend the iterative voting kernel approach to gray level images of cell clusters to combine contour based decomposition of a binary image with local intensity distributions of the corresponding gray level image.

This paper outlines the complete methodology of implementing the radial symmetry technique by means of the iterative voting kernel approach. Several problems that arose within testing the modified method at test images of differing topological features were solved. Virtues and limitations of the radial symmetry decomposition (RSD) technique are explicated and compared with the standard approach of watershed based decomposition (WSD). In this paper promising results of applying the method to complex cell cluster derived with different digitization techniques like bright field microscopy and high resolution transparent flat bed scanning [6] are presented.

2. Material and methods

For the realization, testing and modification of the RSD we use 3 families of images: synthetic images (*arte*) (Fig. 8), light microscopic images of cell clusters (*cells*) [5] and high resolution transparent flat bed scanned images [6] of histological sections of mouse brains stained with the modified method of Gallyas (*scan*) [5,93] (Fig. 9).

Each digital image f is a function that maps discrete coordinates to a finite range of a matrix of the size $m \times n$ leading to an image $I = (f_{i,j})_{i,j=1}^{m,n}$. The image I possesses either gray values or levels $f_{i,j} \in \{0, \dots, 255\}$ denoted as $I_{(g)}$ or two-levels, resp. binary $f_{i,j} \in \{0, 1\}$ that is denoted by $I_{(b)}$. A certain pixel in the image I is denoted by x . More generally, binary $I_{(b)}$ and gray level images $I_{(g)}$ are defined by their ranges \mathbb{B} and \mathbb{G} and the binary image is described by its generating function:

$$b \in \mathbb{B} = \{0, 1\} \quad \text{with } |\mathbb{B}| = B = 2^1, \quad (1)$$

$$g \in \mathbb{G} = \{0, 1, \dots, G-1\} \quad \text{with } |\mathbb{G}| = G = 2^8, \quad (2)$$

$$\mathbb{X} = \{(i, j); i \in \{1, \dots, m\}, j \in \{1, \dots, n\}\}, \quad (3)$$

$$f : \mathbb{X} \rightarrow \mathbb{B} \quad \text{with } f_{i,j} \in \mathbb{B}. \quad (4)$$

Gray level images were segmented by the global segmentation method of Otsu [94] followed by an opening and closing done with a symmetric structure element to remove oversegmented small regions, resp. fill undersegmented small holes.

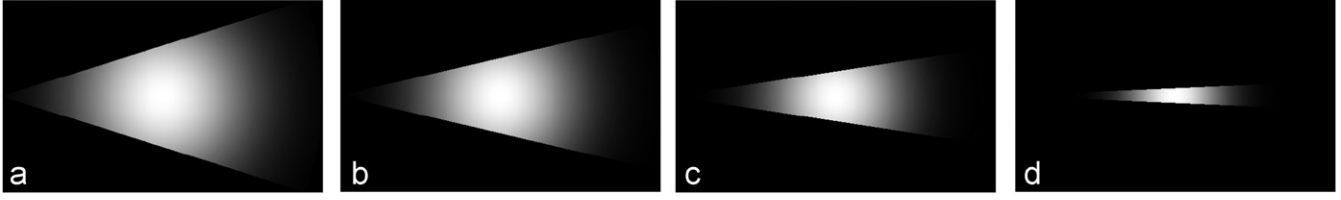


Fig. 2. Kernel topography. Four examples of evolving kernels for the detection of radial symmetries. $D_{max} = 35$. (a) $\sigma = 90$, (b) $\sigma = 80$, (c) $\sigma = 60$, (d) $\sigma = 50$.

Binarianization gives rise to connected components due to juxtaposed objects of interest. Therefore, images are divided in foreground and background. We define the sets $X^1 \subseteq I_{(b)}$ and $X^0 \subseteq I_{(b)}$ with

$$X^1 = \{(i, j) \in \mathbb{X}; f_{i,j} = 1\} \rightarrow \text{foreground}, \quad (5)$$

$$X^0 = \{(i, j) \in \mathbb{X}; f_{i,j} = 0\} \rightarrow \text{background}. \quad (6)$$

Now we state $X^1 \cup X^0 = \mathbb{X}$. The foreground is the union of connected components $X^1 = \bigcup_i X_i^1$. The subset $X_i^1 \subseteq X^1$ is a *connected component* or *object* if the points $x \in X$ of the image f are neighbored within a 8-connectedness of an euclidean metric and that they can be labeled commonly by a certain attribute.

Connected components can be decomposed by the conventional *watershed transformation* [95,96] that is a matter of common knowledge. Therefore, the watershed segmentation is not explained algorithmically. We apply the WSD to compare with the approaches developed here. Since there exist four basic pre-processing steps:

1. directly smoothing the gray level image,
2. distance transformation of a binary segmented image,
3. marker based WSD,
4. internal and external regions approach for applying WSD,

the distance transformation of binary segmented images is used. Finally, the distance transformed images are smoothed by a 5×5 median filter. In the results section the WSD outcomes will be presented first followed by the results of the new techniques.

2.1. Expected decomposition

The expected decompositions (EXD) are considered as the ground truth. They have been generated by human subjects to obtain a set of splittings for comparison with the algorithm results. These splittings are made on principles of Gestalt-theory and perceptive psychology which are broad areas of research in cognitive science where the visual perception and cognition of components of objects are analyzed [97–103]. In cognitive psychology it has been suggested by Attneave [78] that information along visual contours is concentrated in regions of high magnitude of curvature, rather than being distributed uniformly along the contour. Attneave [78] indicates that most shape information is contained in the corners (high curvature points), which are able to characterize the contour. Recently, this has been investigated more precisely by Feldman and Singh [97]

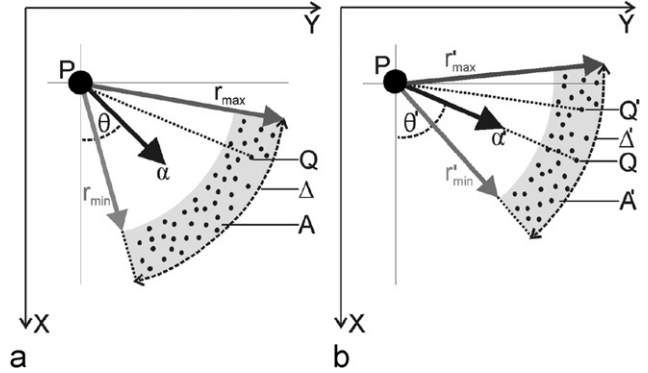


Fig. 3. Reorientation of the kernel at two iterations. (a) In the first iteration the angular range Δ is larger than in (b) the second iteration. Q is a point of A derived from the maximum of the voting area A , resp. the maximum of the voting kernel with regard to P determined at the first iteration. In the second iteration the normal vector, resp. voting direction α is reoriented to Q detected in the last iteration.

in regard to information theory [104,105]. Gestalt theory has shown (based on the Gestalt principles of human perception: proximity, similarity, continuity, closure) that splitting may take advantage of the fact that two sharp inflections must be aligned before clusters are split [106]. Based on these perceptive principles synthetic images exhibiting object agglomerations can be splitted by an investigator to be used for comparison with partitions performed by an algorithm.

2.2. Radial symmetry decomposition

The constitution of cells in brain tissue is rather variable with regard to the size and shape of cells. Therefore, a multiscale technique appears to be proper in order to decompose cell clusters which are composed of highly variable cells. Iterative voting is initialized by voting along the gradient direction where at each iteration (Fig. 5) the voting direction (Fig. 3) and shape of the kernel (Fig. 2) is refined. Let

- $(I_{i,j})_{i,j=1}^{m,n}$ be the original image;
- $(\|\nabla I_{i,j}\|)_{i,j=1}^{m,n}$ be the magnitude of the gradient as a measure of the steepness of the edge independent of its direction that is called here the *voting magnitude*. The magnitude of the gradient is defined in more detail later on;
- $\alpha(i, j)$ be the voting direction, where $\alpha(i, j) := (\cos \theta(i, j), \sin \theta(i, j))$, (Fig. 3). $\theta(i, j)$ is the angle between the positive x -axis and the vector $\alpha(i, j)$;
- r_{min}, r_{max} be the range of radial symmetry (Fig. 3);

- Δ be an angle, monotonically decreased with each iteration step, which determines the width of the kernel;
- the voting area A^+ be

$$A^+(i, j; r_{min}, r_{max}, \Delta) := \left\{ (i + r \cos \phi, j + r \sin \phi) \right. \\ \times |r_{min} \leq r \leq r_{max}, \theta(i, j) \\ \left. - \frac{\Delta}{2} \leq \phi \leq \theta(i, j) + \frac{\Delta}{2} \right\};$$

- after computing the votes of each pixel in every boundary point's voting area which is specified later, the votes are summarized at each iteration step in the voting image $V(i, j; r_{min}, r_{max}, \Delta)$, leading to reorientation. The evolving voting image is shown for two examples at 4 iteration levels in Fig. 7.

The intermediate results of the evolution of the voting landscape at each operation is shown in Fig. 7. In each instance, the voting landscape belonging to a voted image is initially blurred, then subsequently refined and focused into a singular signal. It is reasonable to assume that the center of mass is located along the gradient direction (Eq. (10)) if the process of iterative voting is applied to images without prior knowledge for object locations.

$$\nabla I(i, j) = (\Delta_i I(i, j), \Delta_j I(i, j)), \quad (7)$$

$$\Delta_i I(i, j) = I(i + 1, j) - I(i - 1, j), \quad (8)$$

$$\Delta_j I(i, j) = I(i, j + 1) - I(i, j - 1), \quad (9)$$

$$\theta = \arctan \left(\frac{\Delta_j I(i, j)}{\Delta_i I(i, j)} \right), \quad (10)$$

$$\|\nabla I(i, j)\| = \sqrt{(\Delta_i I(i, j))^2 + (\Delta_j I(i, j))^2}. \quad (11)$$

The discrete gradient magnitude (Eq. (11)) can be assessed by convolution with Gaussian derivatives (Eqs. (13) and (14)). The Gaussian function G_σ is denoted by:

$$G_\sigma(x, y) = \frac{1}{2\pi\sigma^2} e^{-(x^2+y^2/2\sigma^2)}. \quad (12)$$

The partial derivatives of G_σ are given as

$$\frac{\partial}{\partial x} G_\sigma(x, y) = -\frac{x}{2\pi\sigma^4} e^{-(x^2+y^2/2\sigma^2)} \quad (13)$$

$$\frac{\partial}{\partial y} G_\sigma(x, y) = -\frac{y}{2\pi\sigma^4} e^{-(x^2+y^2/2\sigma^2)}. \quad (14)$$

The discrete approximations to the partial derivatives of the Gaussian function (Eq. (12)) lead to suitable masks F_x, F_y to perform the discrete convolution with I (Eqs. (15) and (16)).

Using a $\sigma = 1$, resp. 5×5 kernel size turns out to be an appropriate filter size for approximating the gradient magnitude

image $\|\nabla I(i, j)\|$ (Eq. (18)).

$$\tilde{I}_x(k, l) = \sum_{m=1}^M \sum_{n=1}^N F_x(m, n) I(k + 1 - m, l + 1 - n), \quad (15)$$

$$\tilde{I}_y(k, l) = \sum_{m=1}^M \sum_{n=1}^N F_y(m, n) I(k + 1 - m, l + 1 - n), \quad (16)$$

where $k = 1, \dots, m; l = 1, \dots, n; F_x, F_y$ of size $M \times N$ and zero-padded edges in I are assumed.

To estimate the discrete gradient magnitude we obtain

$$\nabla I(i, j) \approx (\tilde{I}_x(i, j), \tilde{I}_y(i, j)) \quad \text{and so} \quad (17)$$

$$\|\nabla I(i, j)\| \approx \sqrt{(\tilde{I}_x(i, j))^2 + (\tilde{I}_y(i, j))^2} \quad (18)$$

can be determined by discrete approximation.

Eqs. (7)–(18) refer to initial kernel orientation, assumed that the center of mass is located along the gradient direction. Eventually it turned out that reorientation of kernels is necessary to detect centers of radial symmetries, especially when boundaries are not regularly and smooth. Therefore, the kernels represent voting areas for each boundary point. During a single iteration step the votes are accumulated and for each boundary point the new orientation and size of the kernel are derived from the maximum of its voting area.

Since the main intent is to integrate the contribution of each edge location of the contour it is important that boundary points may not be dense and sparsely distributed.

Iterative voting along the gradient direction is influenced by noise and deviation from strict geometric symmetry. To reduce this influence the kernel is refined (Fig. 2) and reoriented (α , Fig. 3) at each consecutive iteration and each edge location. Refinement and reorientation is done along the maximum value in the voting area (Fig. 3). For each point P , if Q is the maximum in the voting area of P , the new voting direction at P is along the direction of \vec{PQ} . The computational cost lies in between $\mathcal{O}(K)$ and $\mathcal{O}(KN \Delta_{max}(r_{max}^2 - r_{min}^2))$ (K : number of pixels in a voting area, N : number of contour points) depending of the image size and shapes of objects [91].

The five parameters of the voting algorithm are considered in more detail. The voting area A can be adapted to the range of intensities where objects are located. The votes can be switched either to bright objects or dark objects or to both of them by changing the signs of Eq. (7). The voting area $A^+(i, j; r_{min}, r_{max}, \Delta)$ (Eq. (7)) for bright objects is defined by

$$A^+(i, j; r_{min}, r_{max}, \Delta) := \left\{ (i + r \cos \phi, j + r \sin \phi) \right. \\ \times |r_{min} \leq r \leq r_{max}, \theta(i, j) \\ \left. - \frac{\Delta}{2} \leq \phi \leq \theta(i, j) + \frac{\Delta}{2} \right\}. \quad (19)$$

In contrast, the voting area $A(i, j; r_{min}, r_{max}, \Delta)$ for dark objects is given by

$$A^-(i, j; r_{min}, r_{max}, \Delta) := \left\{ (i - r \cos \phi, j - r \sin \phi) \right. \\ \times |r_{min} \leq r \leq r_{max}, \theta(i, j) \\ \left. - \frac{\Delta}{2} \leq \phi \leq \theta(i, j) + \frac{\Delta}{2} \right\}. \quad (20)$$

If objects cover bright as well as dark intensity values then bidirectional voting is needed:

$$A^\pm(i, j; r_{min}, r_{max}, \Delta) := A^+(i, j; r_{min}, r_{max}, \Delta) \quad (21)$$

$$\cup A^-(i, j; r_{min}, r_{max}, \Delta). \quad (22)$$

For gray level images the voting magnitude of each pixel is set to the gradient magnitude derived from the convolution with the derivative of a Gaussian. Smooth surfaces are presented by small gradients which can be filtered by introducing a threshold Γ_g . The voting of binary images was performed with a constant magnitude that turns out to be superior because small protrusions of the external contour do not lead anymore to extreme votes.

The radial range can be parametrized by r_{min} , r_{max} and the angular range by Δ_{max} . These parameters are selected due to the shapes of the objects to be detected. If there exist an a priori knowledge about the shapes and if they are constant for instance in images containing clusters of certain geometric forms these parameters can be set easily. To detect a circle we can set $r_{min} = r_{max}$ and $\Delta_{max} = 0$. For an ellipse $x^2/a^2 + y^2/b^2 = 1$ we can use $r_{min} = \min(a, b)$, $r_{max} = \max(a, b)$ and Δ_{max} which is the maximum angle between the radial and the normal vectors (e.g., $\angle OP_1 Q_1$, $\angle OP_2 Q_2$, and $\angle OP_3 Q_3$) by accomplishing $\arcsin |a^2 - b^2|/a^2 + b^2$.

Since the maximum value of the voting area can likely be located at the edge of it, it is essential to adapt r_{min} , and r_{max} to resize the kernel. The aim in defining the new voting area is to cover enough space around the current maximum to allow a convergence in every direction starting from the current maximum. When d is defined as the distance between boundary point and current maximum a shift of $\frac{2}{3} * d$ turned out to be appropriate, concluding in $r_{min} = \frac{1}{3} * d$, and $r_{max} = \frac{5}{3} * d$ as shown in Fig. 4. Hence, the reorientation of the kernel not only involves a possible change of direction but also (very likely) an alteration of size by adapting r_{min} and r_{max} which has decisive influence on the appearance of the voting image as a result from a single iteration step. The absolute changes of the angle for reorientation as well as of the distance from the boundary point tend to be smaller with increasing iterations. This is caused by rising convergence to local signals, supported by a gradually decreased Delta, which makes the kernel successively narrower until it is simply a line in the end.

The number of steps in the evolution of the kernel shape regulates the voting area. If the number of steps is too small, then the centers of mass will be fragmented. If the number of steps is too large, the computational cost will be increased. The monotonically decreased sequence of $\Delta_{max} = \Delta_0 > \Delta_1 > \dots > \Delta_N$ controls the convergence. Updating of the voting direction is

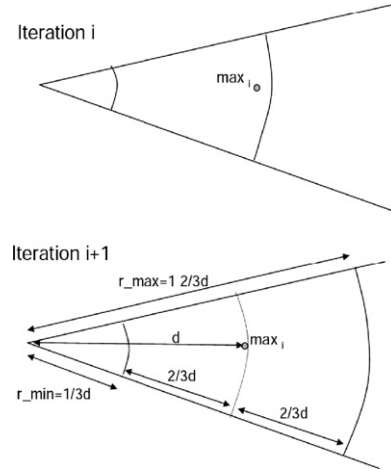


Fig. 4. Resizing the kernel at two iterations. At iteration $i + 1$ r_{max} is adapted to $5/3d$ and r_{min} to $1/3d$.

followed by decreasing the angular range, resp. shrinkage of the voting area. For a circle, $N = 4$ is adequate. If images are noisy, then N should be increased, e.g., $N = 16$.

The voting image presents the voting landscape that is always ranked. Hence, thresholding and local maxima determination may be used to select the most prominent set of hypotheses.

The voting procedure has been adapted to regions containing convex holes. In Figs. 5 and 6 we demonstrate how this is achieved in an example of a region containing one hole. In the first iteration the external contour is voted. If the region contains more than one hole, then the contour of the largest hole is voted first followed by the next smaller hole. Naturally, the process can be applied to many holes and nested structures (not shown here).

The major algorithmic steps are listed as follows:

1. **Initialization:** $\Delta_{max} = \Delta_0 > \Delta_1 > \dots > \Delta_N$
Set $n := 0$, where N is the number of iterations, and let $\Delta_n = \Delta_{max}$.
Determine all boundary points $P = (p, q)$ by tracing the external boundary of regions and holes inside regions in the binary image and store in B . Define r_{min}, r_{max} adapted to each point P . Hence, a binarization and distance transformation of $I_{(b)}$ is required. Along the voting direction, the first local maximum in the distance transformed image is determined. Then $r_{max} := 1.666 \times d$, where d is the distance between the boundary point P and the local maximum. Then $r_{min} := 0.333 \times r_{max}$.
2. **Initialize the voting direction and magnitude:** Regarding the voting direction, one approach for binary and one for gray level images were realized.
Binary images: Consider the averaged perpendicular to boundary point P and two neighbor points and normalize.
Gray level images: Compute the image gradient $\nabla I_{i,j}$, and its magnitude, $\|\nabla I_{i,j}\|$. For each boundary point $(p, q) \in B$, define the voting direction by

$$\alpha(p, q) := \frac{\nabla I_{(p,q)}}{\|\nabla I_{(p,q)}\|}.$$

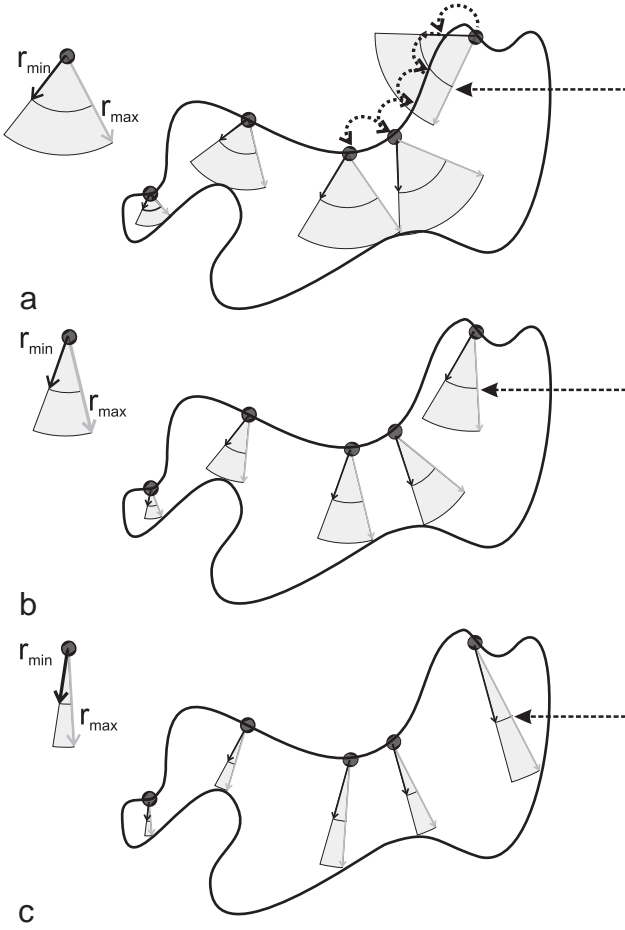


Fig. 5. Three steps of the process of iterative voting. The kernel traverses all coordinates P of the contour (P is a boundary point with coordinates i, j). After one circulation (step) the angular range Δ is decreased. The dashed arrows point to the same α which adapts with respect to orientation at iterations shown in (b) and (c).

3. *Determine the votes:* Reset the vote image $V(i, j; r_{min}, r_{max}, \Delta_n) = 0$ for all pixels (i, j) . For all points $(p, q) \in B$ and $(u, v) \in A(p, q; r_{min}, r_{max}, \Delta_n)$ update the vote image by one of the following voting magnitudes:

(a) For binary images add a constant magnitude $\varepsilon = 1$ to each pixel

$$V(u, v; r_{min}, r_{max}, \Delta_n) := V(u, v; r_{min}, r_{max}, \Delta_n) + \varepsilon.$$

(b) For gray level images add a weighted voting magnitude ε which is composed of the gradient term and the gray value image term each with 0.1. It turns out that for gray images used here $w_1 = 1$ and $w_2 = 3$:

$$\varepsilon(u, v) = w_1 \cdot \frac{\nabla I_{(p,q)}}{\max_{(i,j) \in I} \|\nabla I_{(i,j)}\|} + w_2 \cdot \frac{f_{u,v}}{\max_{(i,j) \in I} f_{i,j}}$$

inserted in

$$V(u, v; r_{min}, r_{max}, \Delta_n) := V(u, v; r_{min}, r_{max}, \Delta_n) + \varepsilon(u, v). \quad (23)$$

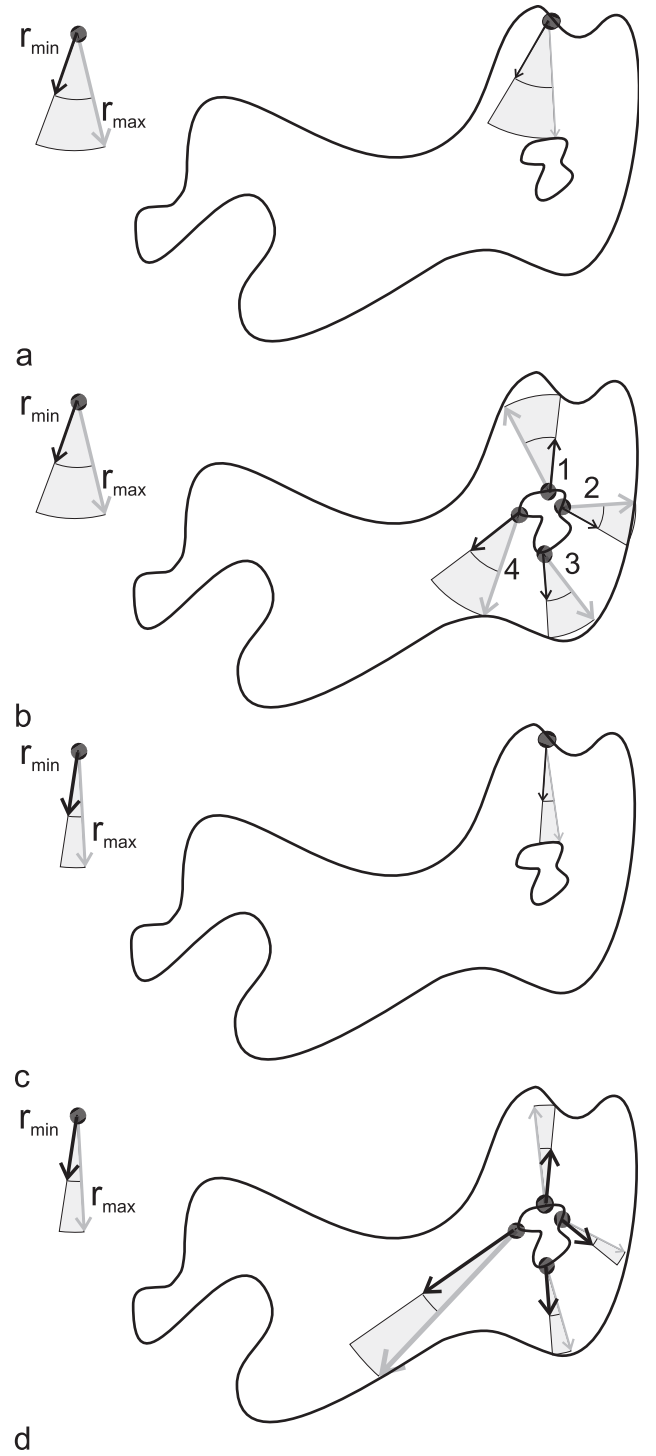


Fig. 6. Two iterations of iterative voting of a region containing a hole. (a) The voting always starts with the first iteration on the external contour. (b) Then the next larger contour contained in the external contour is voted. (c) Then the external contour is voted in the second iteration and followed by voting the hole in (d).

4. *Update the voting direction:* For each boundary point $(i, j) \in B$, revise the voting direction and find

$$Q = (u^*, v^*) = \arg \max_{(u, v) \in A(p, q; r_{min}, r_{max}, \Delta_n)} \{V(u, v; r_{min}, r_{max}, \Delta_n)\} \quad (24)$$

Let $d_p = u^* - p$, $d_q = v^* - q$, and

$$\alpha(p, q) = \frac{(d_p, d_q)}{\sqrt{d_p^2 + d_q^2}}.$$

5. *Update r_{min} and r_{max}* : Set $r_{max} = 1.25 \times d$, where d is the distance between P and Q . The factor 1.25 is chosen due to a better convergence. According to step 1 r_{min} is $0.333 \times r_{max}$.
6. *Refine the angular range*: Let $n := n - 1$, and repeat steps 3–5 until $n = 0$.
7. *Median filtering of the voting landscape*: To avoid oversegmentation the voting landscape arisen during the last iteration step is smoothed by median filtering. The respective size of the filter depends on the size and shape of the region to be decomposed. The compactness or thinness ratio C [9] turns out to be a suitable parameter to describe the shape of a region. It provides a measure of the deviation of a region from an ideal circle where C becomes 1.

$$C = \frac{4\pi \cdot a}{p} \quad \text{with } 0 \leq C \leq 1.$$

The area a is determined considering only the foreground of the region X^1 . The perimeter p results from the exterior boundary supplemented by the boundary of holes. The filter size for median filtering is calculated by $s = c \cdot \sqrt{C \cdot A}$. The constant c should be determined empirically and depends on the size of the image. We obtained optimal results if c is chosen between 0.25 and 0.5.

8. *Postprocessing of the last voting landscape*: In the last smoothed voting landscape the local maxima are determined. These are used as markers for a marker based watershed transformation [95,96,107].

3. Results

In the following the results of the RSD and the WSD in consideration of the EXD are presented.

3.1. Expected decompositions

These partitions are shown in Figs. 7–9. Different persons have partitioned the objects or separated images of cell clusters as shown in Fig. 9. These images are considered as optimal partitions which are compared to the results obtained by EXD and WSD.

3.2. Watershed based decomposition

The four principal preprocessing steps before the watershed algorithm is applied are: (1) binarization and calculating the distance transform, (2) smoothing the gray level image, (3) calculating the gradient image, (4) applying WSD to an image composed of inner and outer markers. In order to facilitate the comparison gray level images were binarized by the same

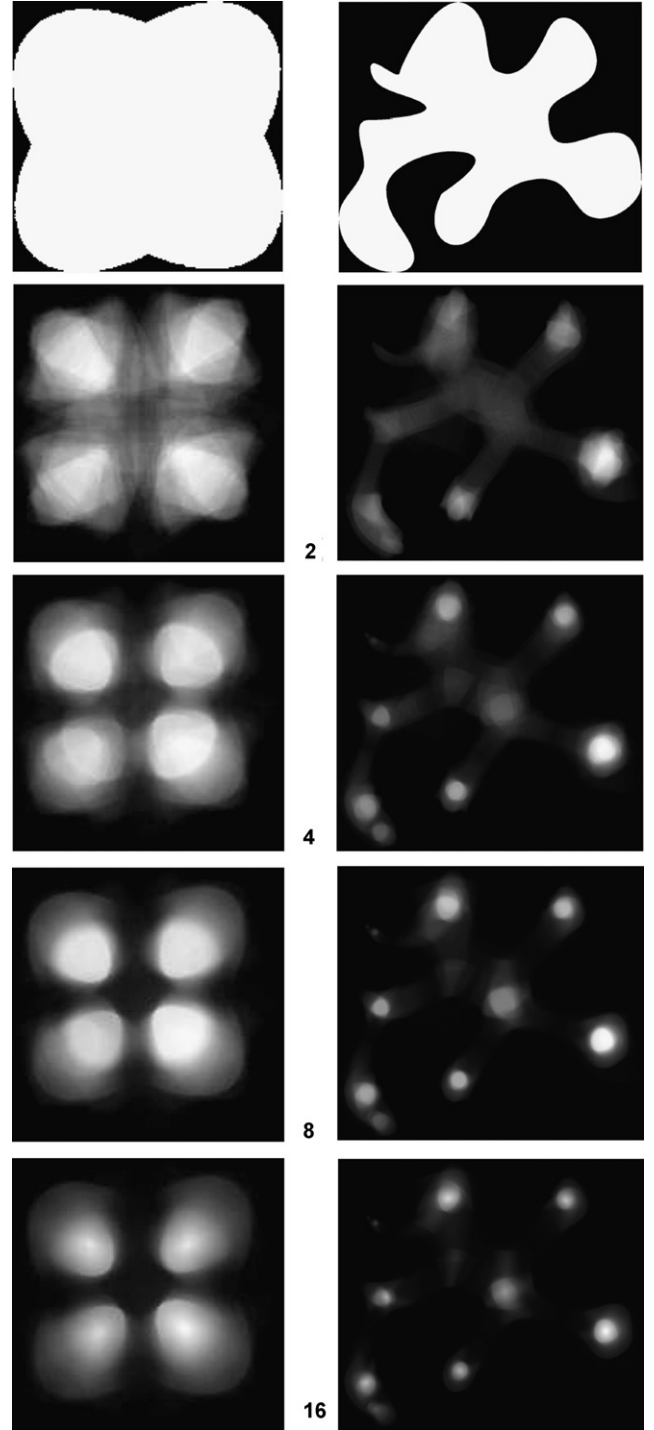


Fig. 7. Two binary images were voted over 16 iterations. Here, we show results after 2, 4, 8 and 16 iterations. The coarse votes are focused to centroids which are processed further on after the voting process.

method as mentioned above followed by the distance and the watershed transformation.

The WSD leads to satisfying results if regions of a connected component do not exhibit too strong overlaps (Figs. 10b, e, k and 11b, e, h, k, n, q, t). However, small subregions positioned around a relative large area (Fig. 11n) and small protrusions with corners (Fig. 11q) produce inadequate results. The WSD

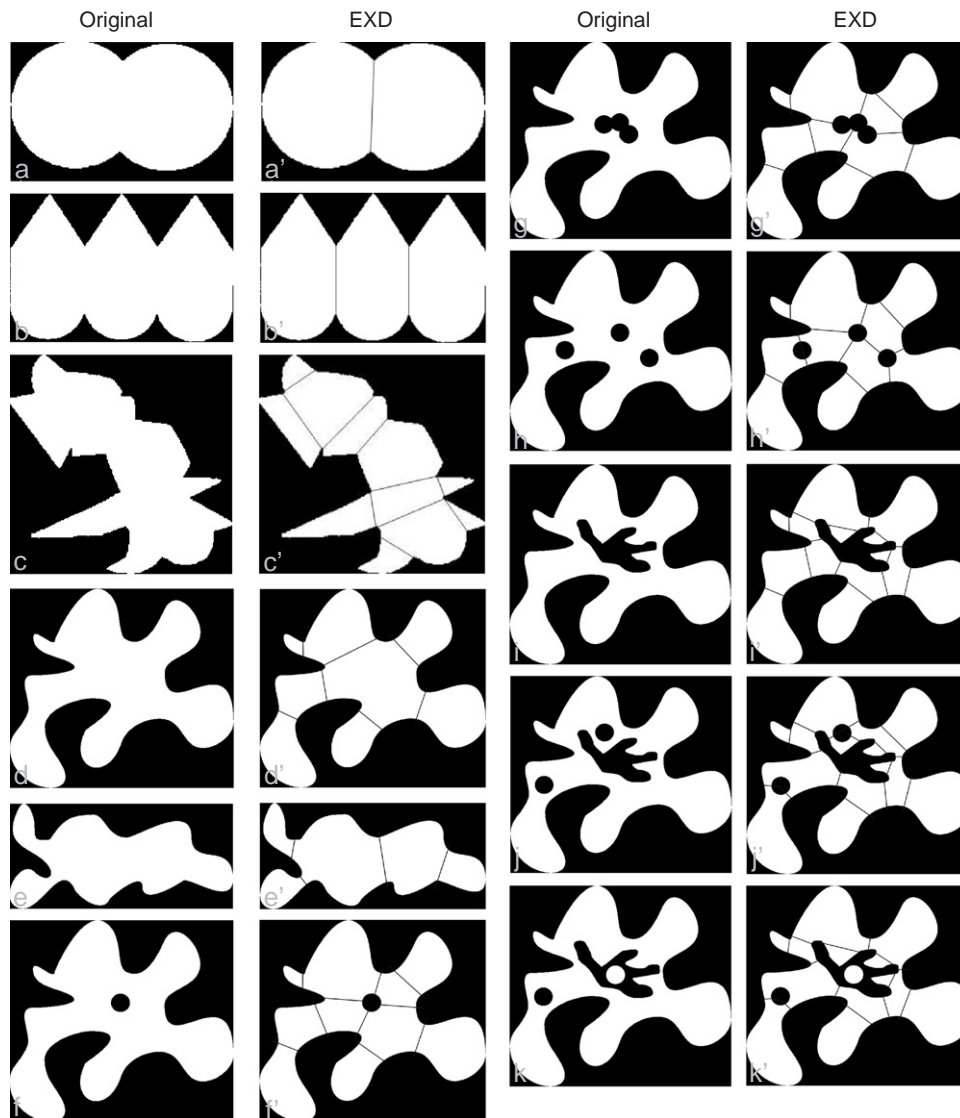


Fig. 8. Synthetic images used for developing and testing the decomposition algorithms. Letters without apostrophe designate the original images and those with an apostrophe the expected decompositions done by investigators. a, b and c are IPAN test images (http://visual.ipan.szaki.hu/-corner/corner_click.html), resp. [108]. In contrast to the IPAN test images we use test images with different kinds of holes and regions within holes.

result of the circle cluster (Fig. 10t) shows a good accordance with the EXD result. Slight oversegmentations were obtained in the synthetic images in Fig. 11k, q and t. Regarding the more complex clusters in Fig. 12b and e we obtain comparable results as observed before. Oversegmentations occur more frequently than undersegmentations. At different regions we find cap-like oversegmentations. Larger objects exhibiting small concavities on their contours are undersegmented. In the scanned mouse brain three cell clusters (Fig. 12k, n, q) were cropped and analyzed separate. The WSD do not produce an appropriate result for this kind of clustering problem.

3.3. Radial symmetries decomposition

The RSD was applied to the same images like EXD and WSD. The synthetic images (Fig. 10a, d, j) show a nearly

perfect match with the EXD results (Fig. 10c, f, l). The image Fig. 10g shows a partial coincidence with the corresponding EXD image Fig. 10i and more splitting paths as those found by WSD. Splitting paths of smaller concavities were not detected. Example Fig. 10m shows a slightly better result as WSD. The airplane example in Fig. 10p shows a better partition as the WSD result. In the circle cluster example in Fig. 10s RSD finds split paths that are well located in between larger touching circles. A perfect result of the RSD in comparison to EXD is shown in Fig. 11a. A nearly perfect match of split paths is presented in Fig. 11d, g, j. In these cases WSD tends to compute split paths oriented parallel to the image borders. The holes are integrated into the split paths and do not disturb iterative voting and calculation of radial symmetries. With the introduction of a concave hole in Fig. 11m the complexity increases. However, several split paths determined by RSD in previous figures

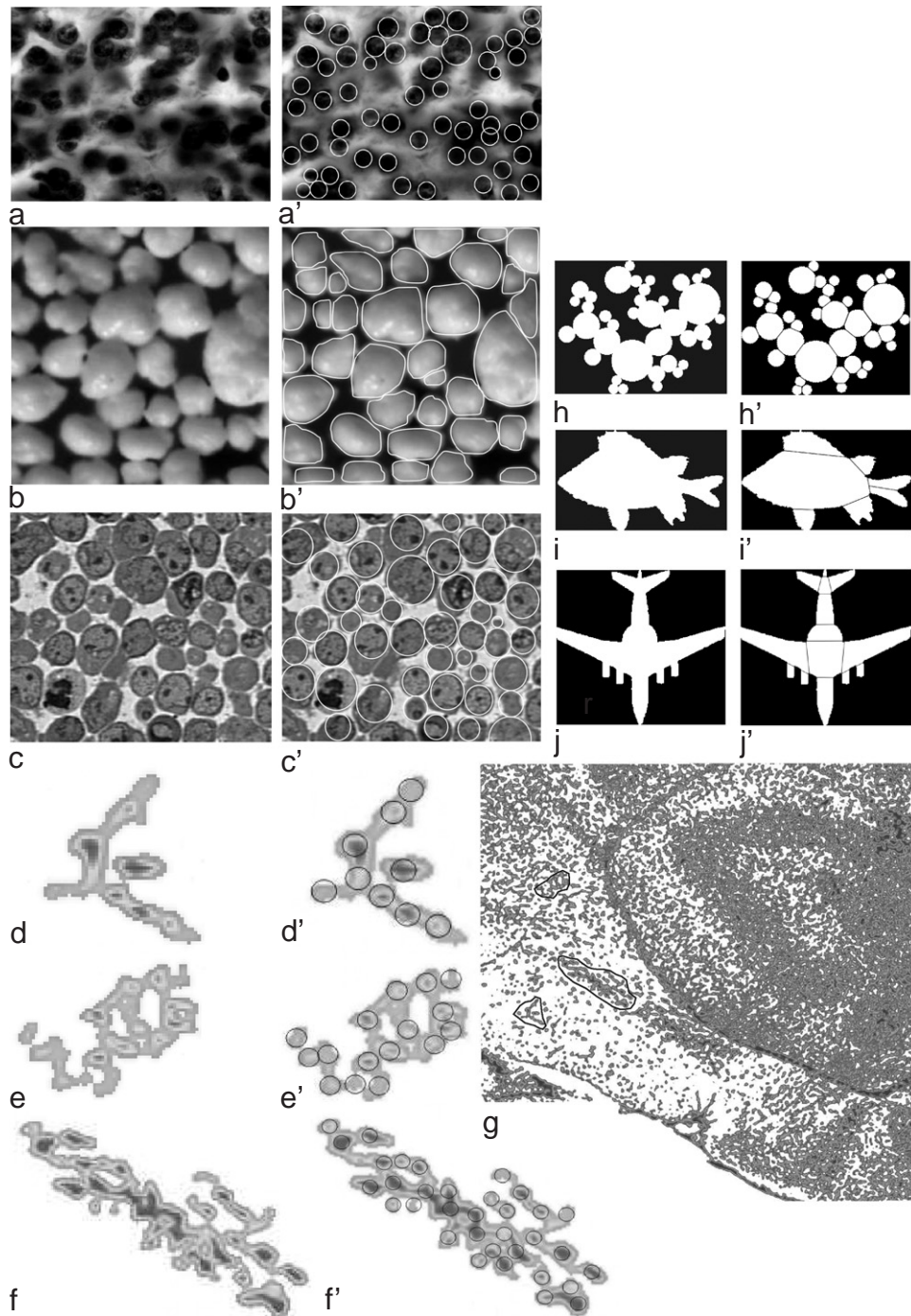


Fig. 9. A micrograph containing cell clusters of the dentate gyrus is shown in (a). (b), (c) and (h) are taken from Russ [109]. With respect to object shape and positioning of objects in (b) and (c) these structures are comparable to cellular objects (taken from Russ [109]). (d)–(f) are high resolution scans of cells from a mouse brain. A part of the scan of a coronal mouse brain section is shown in (g) where the regions are marked by 3 black polygons. (i) and (j) are from the *Squid image database* (<http://www.ee.surrey.ac.uk/Research/VSSP/imagedb/demo.html>) used for shape description algorithms. However, the latter images were contributed originally by Liu and Sclaroff [110]. (http://visual.ipan.szaki.hu/corner/corner_click.html). The expected decompositions are shown on the right side of each original image. Letters without apostrophe designate the original images and those with an apostrophe the expected decompositions done by investigators.

with the same outer boarder are found again. Differences in comparison to the EXD image in Fig. 11o can be observed in between the protrusions of foreground structures into the concave hole. Additional, holes do not disturb RSD (Fig. 11p)

even if a new convex object is located within the concave hole (Fig. 11s).

The decompositions of natural images are presented in Fig. 12. The source images are 8 Bit gray level images that

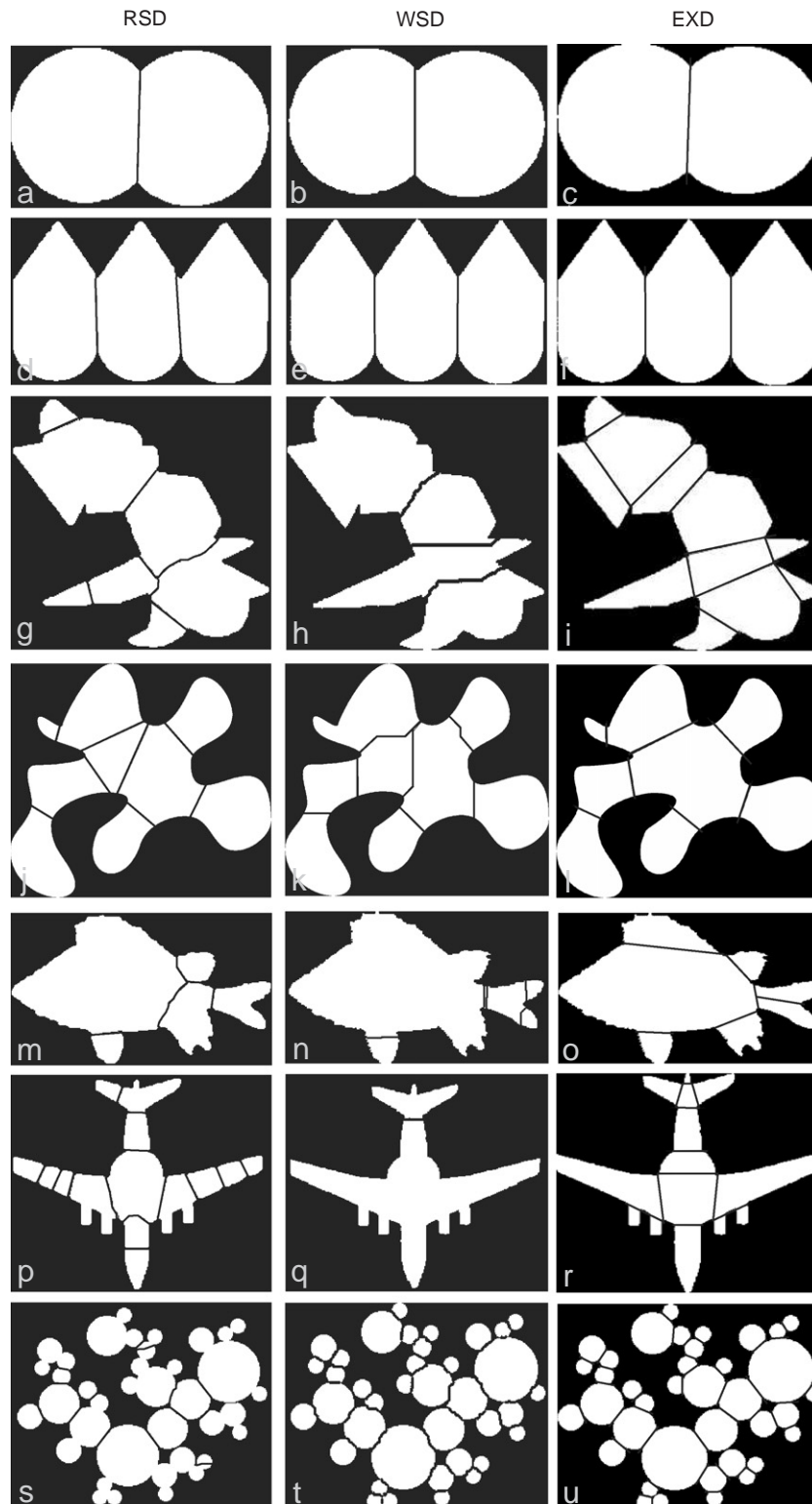


Fig. 10. Results of partitioning by radial symmetry decomposition (RSD) in the first column, watershed decomposition (WSD) in the second column, and expected decomposition (EXD) in the third column. The latter was realized by an evaluator. Here, most images do not possess holes. In (d), (g), (m) and (p) the connected regions exhibit mixtures of corners and continuous concavities. The images (g), (h), (m), (n), (p) and (q) are not partitioned satisfying neither by (WSD) nor (EXD). RSD introduced good splittings in between large circles in (s), however, small circles are subdivided insufficiently.

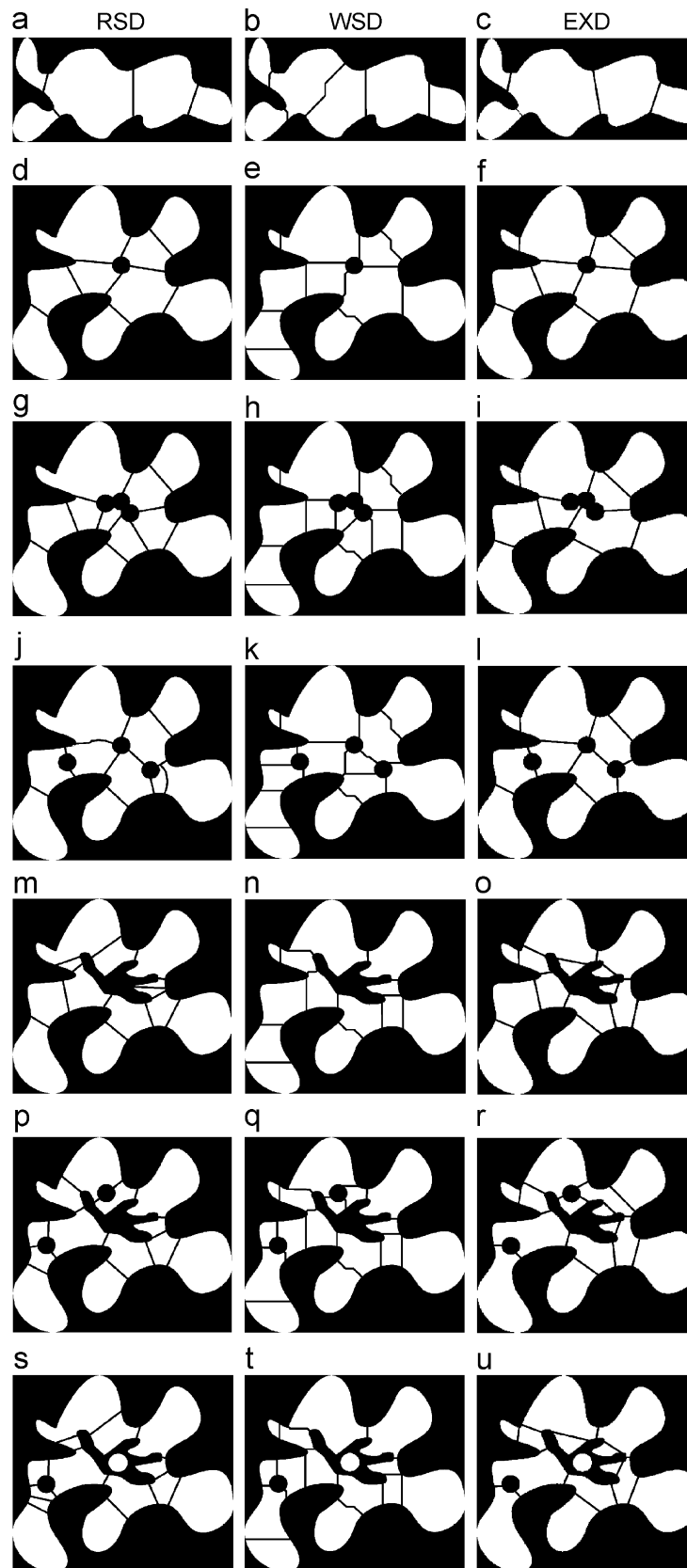


Fig. 11. Analog to Fig. 10 the results of partitioning by radial symmetry decomposition (RSD) are presented in the first column, those of watershed decomposition (WSD) in the second column, and the expected decompositions (EXD) are shown in the third column. As mentioned earlier, the latter was realized by an evaluator. In contrast to the latter figure, most images do possess holes.

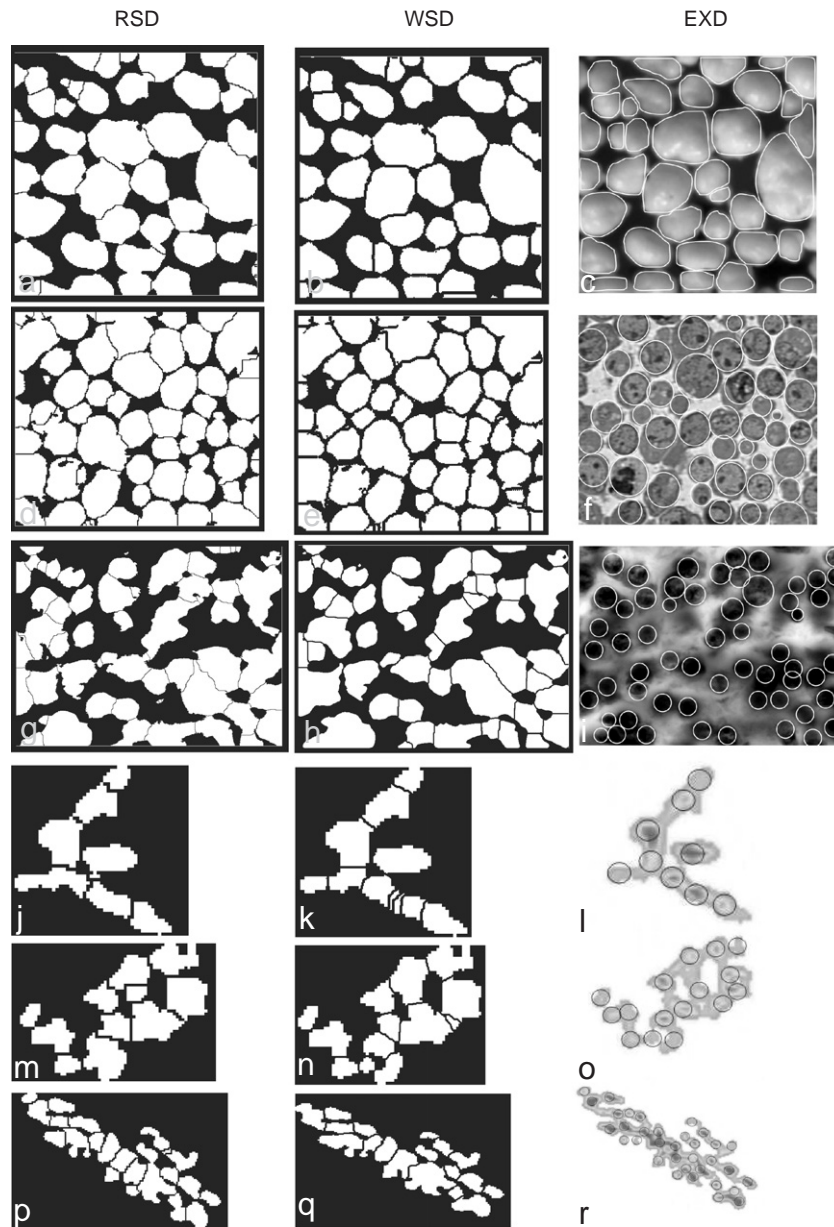


Fig. 12. In the first column the results of the RSD are shown, in the second those of the WSD and those of the last column the EXD and are organized as in Figs. 10 and 11.

were segmented by the Otsu thresholding method [94]. In Fig. 12a–c a better decomposition in comparison to the WSD was obtained. Especially the cluster in the upper left and right corners were partitioned as in the EXD. In the second example (Fig. 12d–f) of an image containing cell clusters RSD detected more partitions and provides a result which is close to the EXD. The WSD result in Fig. 12b shows many partitions which are rather parallel oriented to the image borders. The latter disadvantage is also visible in the third example in Fig. 12h. Here, the RSD comes close to the EXD, however, finer partitions are still absent. The three examples of the small cell clusters derived from high resolution flat bed scanning (Fig. 12j–r) offer problems for the WSD in so far over- and

underpartitions were calculated. In contrast, the RSD approach provides results that are close to the EXD, meaning that the RSD technique can be applied to micrographs (Fig. 12d and g) as well as to high resolution transparent flat bed scans of histological sections of the brain.

Several cases of region clustering can be constructed that reduces the generalization of the RSD. For instance the clustering of relative large and small regular circle objects as shown in Fig. 13. However, in the examples of cell clustering such extreme variations of cell sizes do not occur.

A further improvement of decomposition can be reached by applying the RSD for gray level images as aforementioned. In Figs. 14 and 15 we compared results obtained by RSD applied

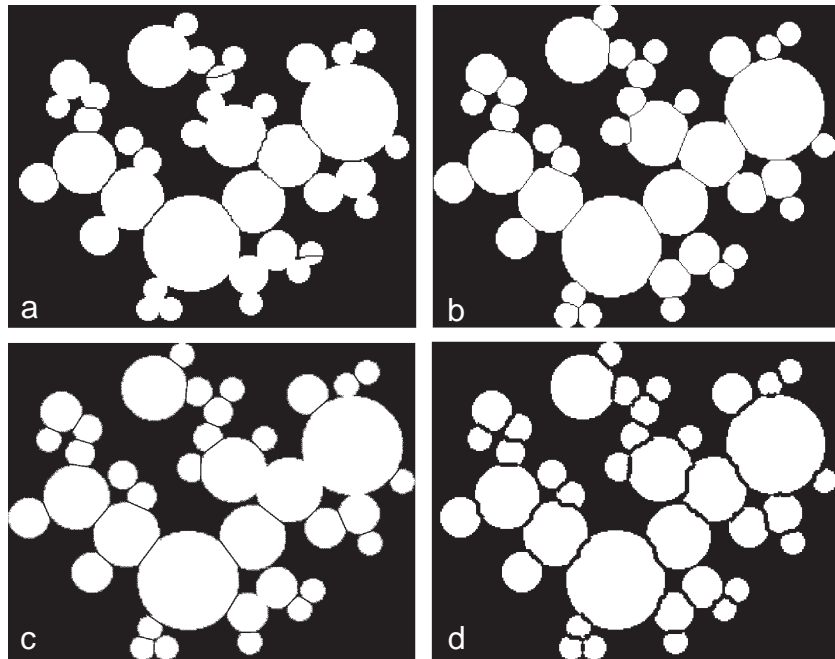


Fig. 13. (a) The result of RSD using an estimate for filtering the centroids of the voting process. (b) The size of the median filter was fitted to the size and shape of the region. (c) The EXD image. (d) The WSD result.

to binarized gray level image and to the same original gray level images. This was done for light microscopic images as well as high resolution scans of mouse brain sections. The voting landscapes at the final iteration are displayed in Figs. 14a, f, k, and 15a, f, k and present obvious convergences around the centroids of the object clusters. The results obtained by applying RSD to gray level images are shown in Figs. 14c, h, m, and 15c, h, m and can be compared with those acquired by applying RSD to binarized images Figs. 14b, g, l, and 15b, g, l. The separation paths are more precise and oversegmentation is reduced. Furthermore, gray level information was used to separate compact objects. This can be verified by comparing the calculated separation paths in Figs. 14d, i, n, and 15d, i, n with the expected object detection images in Figs. 14e, j, o, and 15e, j, o. The benefits of the adaption of the RSD to gray level images are proved also if the resolution is relative low and structures are smoothed which is a feature of scanned mouse brain sections (Fig. 15). In the mouse brain images a superior separation of clustered objects was attained by the gray level approach. Therefore, this technique can be considered as a promising strategy for decomposition of more complex cell clusterings.

4. Discussion

The synthetic images were developed as bilevel images. The gray level images in Fig. 9 were segmented by the method of Otsu [94]. The global segmentation strategy was applied because shading errors do not appear in flat bed scan images and we have optimized microscopic illumination with regard to maximizing homogeneity. Therefore, shading corrections that

effects local gray level distributions were not necessary and local adaptive thresholding was avoided because it turns out to be complex if frame adaption is object size driven. The latter emerge to be problematic due to the high variability of cell cluster sizes which can be presented in multiple tiles of images if larger histological regions (image mosaics) are analyzed.

As described by Metzler et al. [58] and Metzler et al. [46] ultimately eroded points determined by the maximal distance from all adjacent ultimate eroded points are centers of individual objects [111] that can be used for calculating separation lines between them. However, Metzler et al. pointed out that this entails that all objects have to be of similar size and objects must exhibit regular shapes. Hence, compact regions of different size cannot be decomposed correctly because the marker generation depends on size and scale.

The WSD [14–16,18,19,23] is modified, optimized to the specific object segmentation problem and applied by most investigators [14–24]. Since the WSD can be accessed easily because it is implemented in many software packages for image analysis it prevailed for many separation problems. Obvious advantages of the WSD is the applicability to different kinds of preprocessed binary and gray level and color images containing domains to be decomposed which vary within certain ranges in size. At least WSD can be easily adapted to multidimensional partition problems [112].

However, this approach has limitations with regard to cell clusters composed of cells with large differences of cell areas, shapes and center-to-center distances that are smaller than the radius of the assembled objects [23]. Here, we observed problems in terms of holes within clusters of objects. If juxtaposed objects share larger overlapping regions WSD becomes less

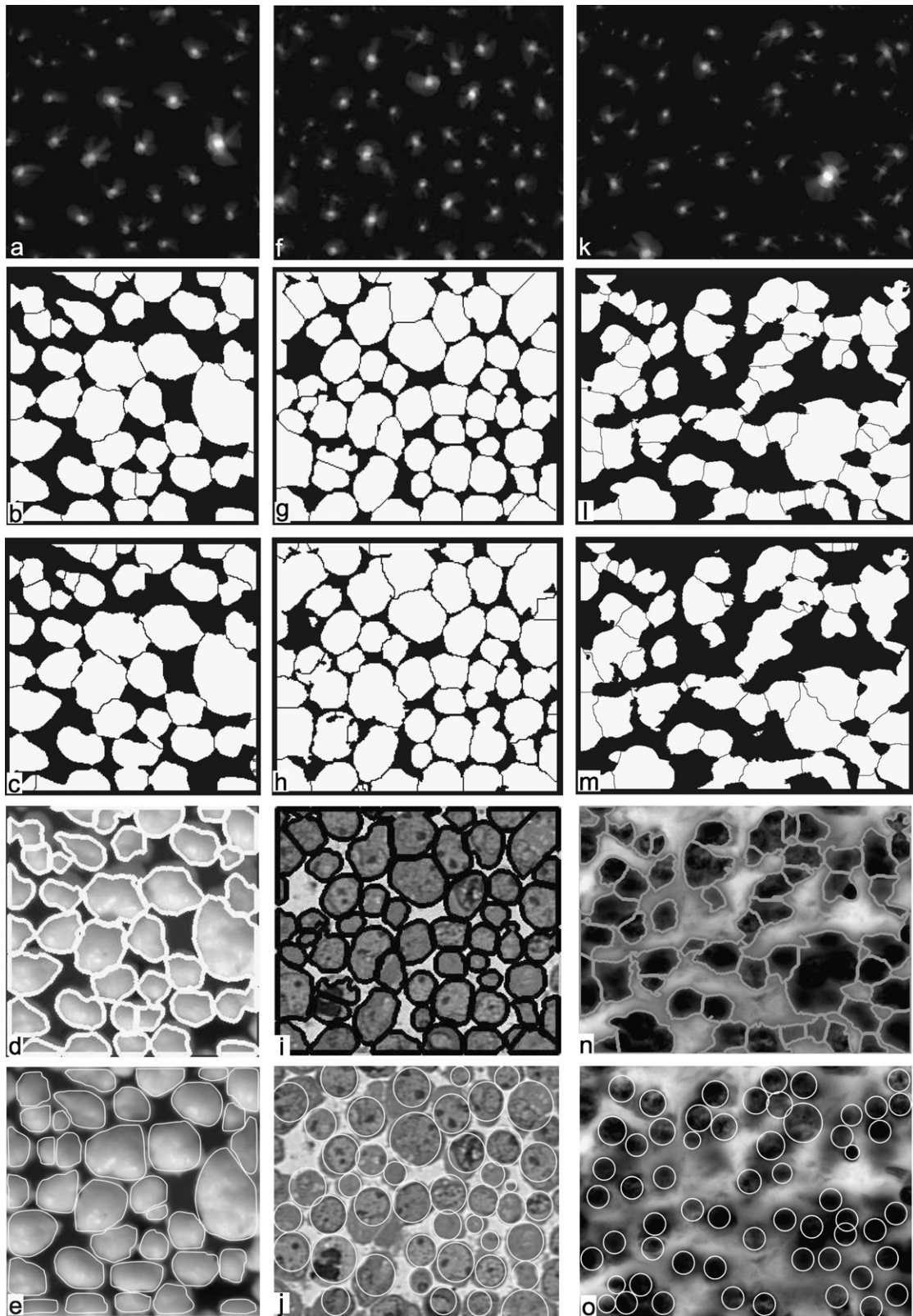


Fig. 14. Comparison of gray and binary image based RSD. Each column belongs to one example. The first line of images (a), (f), (k) shows the voting landscape after the last iteration. The result in terms of a binary visualization of the gray level RSD is shown in image line two: (b), (g), (l). These can be compared with the results of RSD applied to the same, however, binarized images shown in image line three: (c), (h), (m). The decomposition result of the gray level adapted RSD is plotted in the original gray level images in image line four: (d), (i), (n). The latter can be compared with expected results with outlined objects in (e) or marked objects in (j) and (o).

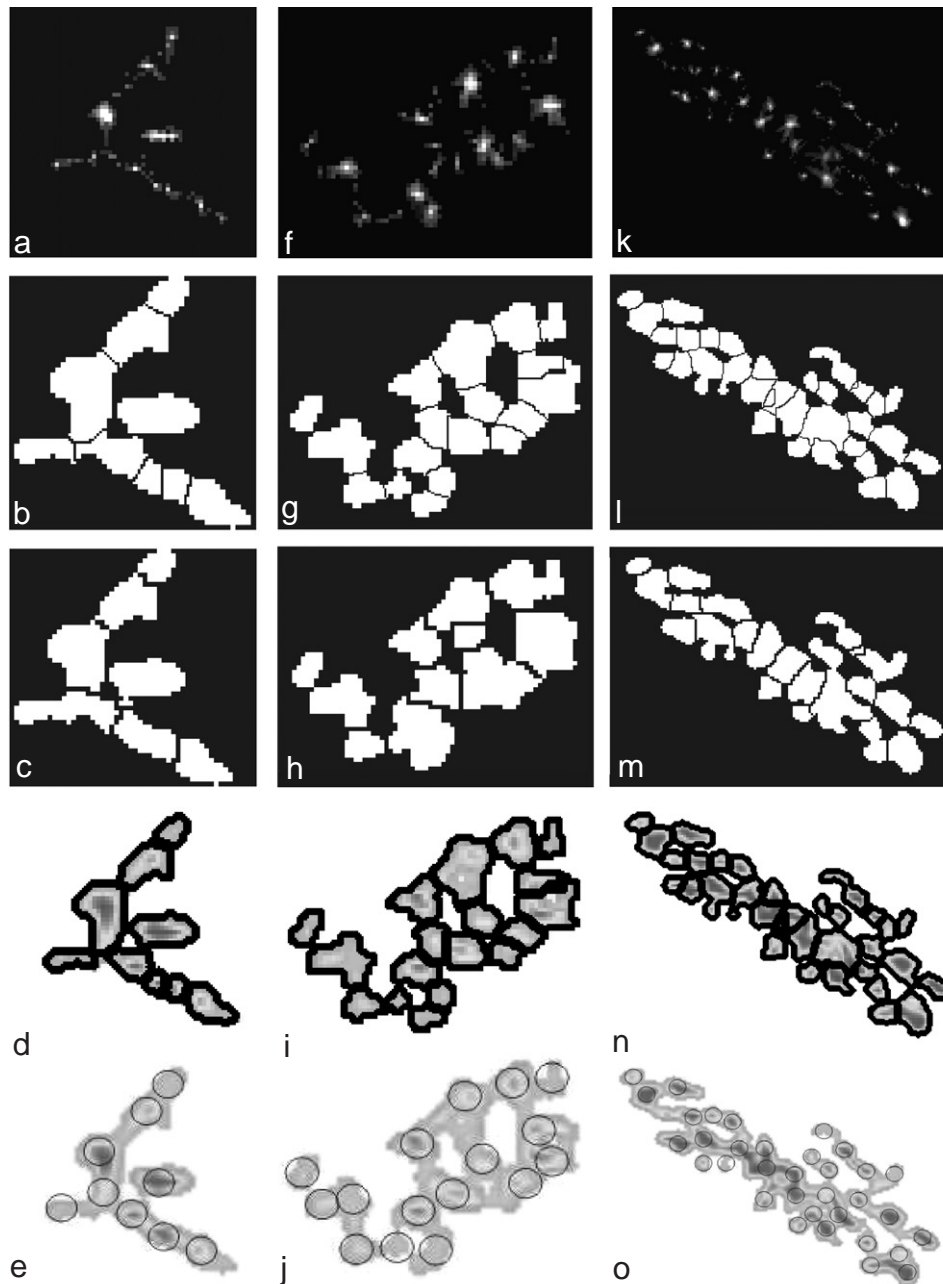


Fig. 15. Comparison of gray and binary image based RSD. Each column belongs to one example. The first line of images (a), (f), (k) shows the voting landscape after the last iteration. The result in terms of a binary visualization of the gray level RSD is shown in image line two: (b), (g), (l). These can be compared with the results of RSD applied to the same, however, binarized images shown in image line three: (c), (h), (m). The decomposition result of the gray level adapted RSD is plotted in the original gray level images in image line four: (d), (i), (n). The latter can be compared with expected results of marked objects (e), (j) and (o).

effective. When WSD is applied to irregularly shaped regions it cause unsatisfying splittings. We observed cap-like separations at large protrusions covering small areas. Another disadvantage is that inaccurate split paths are placed around concavities not passing them exactly. Overall, WSD clearly exhibits obvious differences to the EXD. With respect to decomposition problems of a larger class of planar domains WSD turns out to be inappropriate.

The iterative voting of radial symmetries avoids the drawbacks due to irregular shaped regions, large and long protrusions covering small areas and inaccurate positioning of split paths mentioned before. These disadvantages of the watershed technique result mainly from its single-scale nature. The generation of a morphological scale-space, filtering of false markers, and their stepwise reconstruction is independent of the object's size and additionally improve results.

An important improvement was achieved by adapting the RSD working on binarized images to gray level images. We have shown in numerous examples of varying complexity derived from different imaging modalities that the gray level RSD generates superior decompositions. Therefore, this new approach can be recommended for complex decomposition tasks.

The RSD can be applied successfully to object compositions with strong discontinuities or corners. Especially, shapes that are elongated or where objects are clustered in a circular- [113] chain- and cluster-like manner [114] can be partitioned efficiently by the RSD. The result and cost of the RSD algorithm can be controlled by choosing a suitable sampling size of the contour and appropriate smoothing before iterative voting starts. Furthermore, the kernel topography (Fig. 2) can be adapted to the shape of particle to be partitioned. One limitation of the RSD is the prior knowledge of scale which cannot be generalized. To overcome this limitation multiscale extension of the iterative voting of radial symmetries seems to be reasonable. A further aspect is the completeness since the method infers potential centers of mass in an image of a given scale. These inferences need to be verified by yet another higher level process. In comparison to the approach of Yang et al. [113] and Yang and Parvin [91] we have coupled the result of iterative voting of radial symmetries with subsequent marker based watershed segmentation. The markers used by the watershed post-processing are of course those found by iterative voting. Hence, we speak of radial symmetry based *decomposition* which is a three step technique of preprocessing, iterative voting and post-processing, i.e., watershed separation of the last voting landscape. Needless to say that this type of postprocessing can be replaced by other techniques.

Finally, we would like to point out that centers of mass determined by iterative passing the contour using appropriate kernels can be determined by other methods as well, which are geometrical calculation of gravity centers of binary objects and local symmetry approaches [81,84]. Local orientation techniques may turn out to be suitable as well with regard to local singularities in gradient images [82,115,116].

We intend to solve partitions of strongly clustered cells of different size and shape which may come up to huge and highly complex clusters like that shown in Fig. 9g the WSD is not suitable in terms of reliability. It turns out that the new RSD approach offers some important advantages with regard to partitioning of objects covering features of

- convex and concave corners;
- convex and concave curves;
- geometric hierarchies of concavities and convexities;
- domains with holes within clusters of objects.

An important feature of the RSD is its reliability with regard to similar split paths if holes are added to the same cluster of objects. It was shown that objects with strong discontinuities like the example of the binary plane and the binary fish result in partitions that are rather similar like those derived from EXD.

It is now clear that, in addition to strong overlaps of domains containing multiple holes (Fig. 11d–u) that such subregions

of a connected component can be integrated into meaningful partitions. This observation suggests, that compared to other studies the RSD approach has some principal advantages concerning partition of clustered regions with emerging complexity. At this point of time, however, it has not been possible to identify clearly single cells in huge clusters of several thousands of cells each composed of a few pixels which are derived from high resolution flat bed scanning. Therefore, this issue is considered currently by developing pre-partitioning steps and parallelized algorithms. We have presented experimental data that the RSD approach, while not definitive, will provide a useful perspective for future investigations of decomposing highly complex aggregations of biological cells.

References

- [1] O. Schmitt, R. Eggers, Systematic investigations of the contrast results of histochemical stainings of neurons and glial cells in the human brain by means of image analysis, *Micron* 28 (1997) 197–215.
- [2] S. Ong, Image analysis of tissue sections, *Comput. Biol. Med.* 26 (1996) 269–279.
- [3] P. Adiga, B. Chaudhuri, K. Rodenacker, Semi-automatic segmentation of tissue cells from confocal microscope images, in: *ICPR'96*, 1996, pp. 494–497.
- [4] H. Ancin, B. Roysam, T. Dufresne, M. Chestnut, G. Ridder, D. Szarowski, J. Turner, Advances in automated 3-D image analyses of cell populations imaged by confocal microscopy, *Cytometry* 25 (1996) 221–234.
- [5] O. Schmitt, R. Eggers, J. Modersitzki, Videomicroscopy, image processing, and analysis of whole histologic sections of the human brain, *Microsc. Res. Tech.* 66 (2005) 203–218.
- [6] O. Schmitt, R. Eggers, Flat-bed scanning as a tool for quantitative neuroimaging, *J. Microsc.* 196 (1999) 337–346.
- [7] D. Zhang, G. Lu, Review of shape representation and description techniques, *Pattern Recognition* 37 (2004) 1–19.
- [8] K. Rodenacker, E. Bengtsson, A feature set for cytometry on digitized microscopic images, *Anal. Cell Pathol.* 25 (2003) 1–36.
- [9] L. Costa, R.M. Cesar, *Shape Analysis and Classification*, CRC Press, Boca Raton, 2001.
- [10] S. Pizer, D. Fritsch, P. Yushkevich, V. Johnson, E. Chaney, Segmentation, registration, and measurement of shape variation via image object shape, *IEEE Trans. Med. Image* 18 (1999) 851–865.
- [11] S. Loncaric, A survey of shape analysis techniques, *Pattern Recognition* 31 (1998) 983–1001.
- [12] D. Foran, R. Berg, A method for quantitative image assessment based on redundant feature measurements and statistical reasoning, *Comput. Methods Programs Biomed.* 45 (1994) 291–305.
- [13] C. Xiaohua, Y. Chang, Application of some valid methods in cell segmentation, *SPIE J.* 4550 (2001) 340–344.
- [14] C. Wahlby, I.-M. Sintorn, F. Erlandsson, G. Borgefors, B. Bengtsson, Combining intensity, edge and shape information for 2D and 3D segmentation of cell nuclei in tissue sections, *J. Microsc.* 215 (2004) 67–76.
- [15] E. Bengtsson, C. Wahlby, J. Lindblad, Robust cell image segmentation methods, *Pattern Recognition Image Anal.* 14 (2004) 157–167.
- [16] C. Wahlby, E. Bengtsson, Segmentation of cell nuclei in tissue by combining seeded watersheds with gradient information, *Lecture Notes in Computer Science*, vol. 2749, Springer, Berlin, 2003, pp. 408–414.
- [17] C. Loukas, G. Wilson, B. Vojnovic, Automated segmentation of cancer cell nuclei in complex tissue sections, *SPIE J.* 4158 (2001) 188–198.
- [18] B. Nilsson, A. Heyden, Segmentation of dense leukocyte clusters, in: *Proceedings of MMBIA*, vol. 1, 2001, pp. 221–227.
- [19] Y. Cui, N. Zhou, Blob analysis using watershed transformation, *Lecture Notes in Artificial Intelligence*, vol. 1821, 2000, pp. 482–491.

- [20] J. Costa, D. Mascarenhas, L. Marcio, M. de Andrade Netto, Cell nuclei segmentation in noisy images using morphological watersheds, *SPIE J.* 3164 (1997) 314–324.
- [21] P. van Ham, C. de Hauwer, R. Kiss, Dynamic behaviour analysis of in vitro cancerous cells by means of an automatic image processing device, *SPIE J.* 2710 (1996) 967–978.
- [22] H. Ancin, T.E. Dufresne, G.M. Ridder, J.N. Turner, B. Roysam, An improved watershed algorithm for counting objects in noisy, anisotropic 3-D biological images, in: *ICIP '95: Proceedings of the 1995 International Conference on Image Processing*, vol. 3, IEEE Computer Society, Washington, DC, USA, 1995, p. 3172.
- [23] Y.-K. Lee, J.-H. Kim, An efficient morphological segmentation for significantly overlapped particles, *SPIE J.* 2424 (1995) 349–357.
- [24] A. Dow, S. Shafer, A. Waggoner, Morphological segmentation of multi-probe fluorescence images for immunophenotyping in melanoma tissue sections, *SPIE J.* 2055 (1993) 487–498.
- [25] T. Pavlidis, S. Horowitz, Segmentation of plane curves, *IEEE Trans. Comput.* 23 (1974) 860–870.
- [26] E.E. Gose, W.H. Rose, W.E. Barnes, E. Kaplan, J.S. Arnold, Decomposition of image sequences of overlapping homogeneous transparent radiating objects, in: *A Comparison of Some Segmentation Algorithms for Cytology*, 1980, pp. 971–973.
- [27] S. Grinaker, Edge based segmentation and texture separation, in: *A Comparison of Some Segmentation Algorithms for Cytology*, 1980, pp. 554–557.
- [28] G.G. Pieroni, M.F. Costabile, G. Guerra, Decomposition of shape boundaries in a problem of map sequence analysis, in: *A Comparison of Some Segmentation Algorithms for Cytology*, 1980, pp. 618–623.
- [29] J. Rowinski, C. Souchier, J. Czyba, M. Pages, R. Fages, J. Laurent, T. Greenland, Morphometric studies of cell nuclei by means of image analysis and computer data processing, *Gegenbaurs Morph. Jahrb.* 126 (1980) 253–263.
- [30] S. Serpico, G. Vernazza, S. Dellepiane, Merging of different segmentation techniques for cell image recognition, *SPIE J.* 1027 (1988) 208–213.
- [31] D. Thompson, H. Bartels, J. Haddad, P. Bartels, Scene segmentation in a machine vision system for histopathology, *SPIE J.* 1206 (1990) 40–47.
- [32] O. Stephansson, W. Wang, S. Dahlhielm, Automatic image processing of aggregates, in: *ISRM Symposium: Eurock'92*, 1992, pp. 31–35.
- [33] T. Yeo, X. Jin, S. Ong, S. Jayasooriah, R. Sinniah, Clump splitting through concavity analysis, *Pattern Recognition Lett.* 15 (1994) 1013–1018.
- [34] R. Malladi, *Geometric Methods in Bio-medical Image Processing*, Springer, Berlin, 2001.
- [35] P. Bamford, P. Jackway, B. Lovell, Progress in the robust automated segmentation of real cell images, *SPIE J.* 3747 (1999) 34–56.
- [36] J. Modersitzki, *Numerical Methods for Image Registration*, Oxford University Press, Oxford, 2004.
- [37] M. Szezin, B. Sankur, Survey over image thresholding techniques and quantitative performance evaluation, *J Electron. Imaging* 13 (2007) 146–165.
- [38] Y. Zhang, Evaluation and comparison of different segmentation algorithms, *Pattern Recognition Lett.* 18 (1997) 963–974.
- [39] N. Pal, S. Pal, A review on image segmentation techniques, *Pattern Recognition* 26 (1993) 1277–1294.
- [40] P. Sahoo, S. Soltani, A. Wong, Y. Chen, A survey of thresholding techniques, *CVGIP* 41 (1988) 233–260.
- [41] R. Haralick, L. Shapiro, *Image segmentation techniques*, *CVGIP* 29 (1985) 100–132.
- [42] J. Weszka, A survey of threshold selection techniques, *CGIP* 7 (1978) 259–265.
- [43] Q. Wei, C. Reme, P. Stucki, Advanced image processing and modeling system for the analysis of cell micrographs in morphology, *SPIE J.* 1905 (1993) 175–185.
- [44] A. Elmoataz, S. Schupp, R. Clouard, P. Herlin, D. Bloyet, Using active contours and mathematical morphology tools for quantification of immunohistochemical images, *Signal. Process.* 71 (1998) 215–226.
- [45] S. Portet, J. Vassy, M. Beil, G. Millot, A. Hebbache, J. Rigault, D. Schoevaert, Quantitative analysis of cytokeratin network topology in the MCG7 cell line, *Cytometry* 35 (1999) 203–213.
- [46] V. Metzler, T. Lehmann, H. Bienert, K. Mottaghy, K. Spitzer, Scale-independent shape analysis for quantitative cytology using mathematical morphology, *Comput. Biol. Med.* 30 (2000) 135–151.
- [47] P. Maragos, R. Schaffer, Morphological filters—part II: their relation to median, order-statistic, and stack filters, *IEEE Trans. Acoust. Speech Signal Process* 35 (1987) 1170–1184.
- [48] H. Heijmans, Mathematical morphology as a tool for shape description, *Shape in Picture: Mathematical Description of Shape in Grey-level Images*, Springer, Berlin, 1994, pp. 147–176 (chapter).
- [49] P. Maragos, Pattern spectrum and multiscale shape representation, *IEEE Trans. PAMI* 11 (1989) 701–716.
- [50] J. Reinhardt, W. Higgins, Comparison between the morphological skeleton and morphological shape decomposition, *IEEE Trans. PAMI* 18 (1996) 951–957.
- [51] P. Salembier, M. Kunt, Size-sensitive multiresolution decomposition of images with rank-order based filters, *Signal Process.* 27 (1992) 205–241.
- [52] J. Goutsias, H. Heijmans, Multiresolution signal decomposition schemes. Part 1: Linear and morphological pyramids, *IEEE Trans. Image Process.* 9 (2000) 1862–1876.
- [53] H. Heijmans, R. van den Boomgaard, Algebraic framework for linear and morphological scale-spaces, *J. Math. Image Vision* 13 (2002) 269–301.
- [54] H. Talbot, B. Appleton, Elliptical distance transforms and the object splitting problem, in: *Proceedings of ISMM2002*, 2002, pp. 229–240.
- [55] J. Lindblad, C. Wählby, E. Bengtsson, A. Zaltsman, Image analysis for automatic segmentation of cytoplasm and classification of Rac1 activation, *Cytometry* 57 (2004) 22–33.
- [56] G. Lin, M. Chawia, K. Olson, J. Guzowski, C. Barnes, B. Roysam, Hierarchical, model-based merging of multiple fragments for improved three-dimensional segmentation of nuclei, *Cytometry* 63 (2004) 20–33.
- [57] E. Bengtsson, Computerized cell image analysis: past present, and future, *Lecture Notes in Computer Science*, vol. 2749, Springer, Berlin, 2003, pp. 395–407.
- [58] V. Metzler, T. Lehmann, T. Aach, Morphological multiscale shape analysis of light micrographs, *SPIE J.* 3961 (2000) 227–238.
- [59] A. Nedzved, S. Ablameyko, I. Pitas, Morphological segmentation of histology cell images, *ICPR* 1 (2000) 1500–1504.
- [60] M. Marji, P. Siy, Polygonal representation of digital planar curves through dominant point detection—a nonparametric algorithm, *Pattern Recognition* 37 (2004) 2113–2130.
- [61] T. Cronin, Visualizing concave and convex partitioning of 2D contours, *Pattern Recognition Lett.* 24 (2003) 429–443.
- [62] M. Tănase, R. Veltkamp, Polygon decomposition based on the straight line skeleton, *SoCG* 1 (2003) 58–67.
- [63] Q. Yang, B. Parvin, Harmonic cut and regularized centroid transform for localization of subcellular structures, *IEEE Trans. Biomed. Eng.* 50 (2003) 469–475.
- [64] G.-A. Bilodeau, Part segmentation of objects in real images, *Pattern Recognition* 35 (2002) 2913–2926.
- [65] T. Lee, M. Atkins, Z.-N. Li, Indentation and protrusion detection and its applications, *Lecture Notes in Computer Science*, vol. 2106, Springer, Berlin, 2001, pp. 335–343.
- [66] M. Salotti, An efficient algorithm for the optimal polygonal approximation of digitized curves, *Pattern Recognition Lett.* 22 (2001) 215–221.
- [67] J. Shah, 2001. Segmentation of shapes, *Lecture Notes in Computer Science*, vol. 2106, Springer, Berlin, 2001, pp. 236–244.
- [68] T. Lee, M. Atkins, A new approach to measure border irregularity for melanocytic lesions, *SPIE J.* 3979 (2000) 668–675.
- [69] P. Rosin, Shape partitioning by convexity, *IEEE Trans. Syst. Man Cybern.—Part A* 30 (2000) 202–210.
- [70] W. Clocksin, Automatic segmentation of overlapping nuclei with high background variation using robust estimation and flexible contour models, in: *ICIAIP*, vol. 1, 2003, pp. 682–687.
- [71] S. Sclaroff, L. Liu, Deformable shape detection and description via model-based region grouping, *IEEE Trans. PAMI* 23 (2001) 475–489.
- [72] J.M. Geusebroek, A.W.M. Smeulders, F. Cornelissen, H. Geerts, Segmentation of tissue architecture by distance graph matching, *Cytometry* 35 (1999) 12–22.

- [73] J.M. Geusebroek, A.W.M. Smeulders, F. Cornelissen, Segmentation of cell clusters by nearest neighbour graphs, in: *ASCI'97, Proceedings of the Third Annual Conference of the Advanced School for Computing and Imaging*, 1997, pp. 248–252.
- [74] E. Dejnokova, P. Dokladal, Modelling of overlapping circular objects based on level set approach, *Lecture Notes in Computer Science*, vol. 3211, Springer, Berlin, 2004, pp. 416–423.
- [75] F. Yang, T. Jiang, Cell image segmentation with kernel-based dynamic clustering and an ellipsoidal cell shape model, *J. Biomed. Inf.* 34 (2001) 67–73.
- [76] H.-S. Wu, J. Barba, J. Gil, A parametric fitting algorithm for segmentation of cell images, *IEEE Trans. Biomed. Eng.* 45 (1998) 400–407.
- [77] S. Schüpp, A. Elmoataz, M.-J. Fadili, D. Bloyet, 2001. Fast statistical level sets image segmentation for biomedical applications, *Lecture Notes in Computer Science*, vol. 2106, Springer, Berlin, 2001, pp. 380–388.
- [78] F. Attneave, Some informational aspects of visual perception, *Psychol. Rev.* 61 (1954) 183–193.
- [79] M. Mellor, M. Brady, A new technique for local symmetry estimation, in: *Lecture Notes in Computer Science*, Springer, Berlin, 2005, pp. 38–49.
- [80] Y. Liu, R. Collins, Y. Tsing, A computational model for periodic pattern perception based on frieze and wallpaper groups, *IEEE Trans. PAMI* 26 (2004) 354–371.
- [81] G. Loy, A. Zelinsky, Fast radial symmetry for detecting points of interest, *IEEE Trans. PAMI* 25 (2003) 959–973.
- [82] B. Johansson, H. Knutsson, G. Granlund, Detecting rotational symmetries using normalized convolution, in: *ICPR, 2000*, pp. 3500–3504.
- [83] H. Zabrodsky, S. Peleg, D. Avnir, Symmetry as a continuous feature, *IEEE Trans. PAMI* 17 (1995) 1154–1166.
- [84] D. Reisfeld, H. Wolfson, Y. Yeshurun, Context-free attentional operators: the generalized symmetry transform, *IJCV* 14 (1995) 119.
- [85] D. Reisfeld, Y. Yeshurun, Preprocessing of face images: detection of features and pose normalization, *CVIU* 71 (1998) 13.
- [86] G. Sela, M. Levine, Real-time attention for robotic vision, *Real-time Imaging* 3 (1997) 173–194.
- [87] V. Leavers, *Shape Detection in Computer Vision using the Hough Transform*, Springer, Berlin, 1992.
- [88] Q. Yang, B. Parvin, Harmonic cut and regularized centroid transform for localization of subcellular structures, in: *ICPR '02: Proceedings of the 16th International Conference on Pattern Recognition (ICPR'02)*, vol. 1, IEEE Computer Society, Washington, DC, USA, 2002, pp. 788–791.
- [89] B. Parvin, Q. Yang, G. Fontenay, M. Barcellos-Hoff, BioSig: an imaging bioinformatic system for studying phenomic, *Computer* 35 (2002) 65–71.
- [90] B. Parvin, G. Cong, G. Fontenay, J. Taylor, R. Henshall, M.H. Barcellos-Hoff, BioSig: a bioinformatic system for studying the mechanism of inter-cell signaling, in: *BIBE '00: Proceedings of the 1st IEEE International Symposium on Bioinformatics and Biomedical Engineering*, IEEE Computer Society, Washington, DC, USA, 2000, pp. 281–288.
- [91] Q. Yang, B. Parvin, Perceptual organization of radial symmetries, *CVPR*, vol. 1, 2004, pp. 320–325.
- [92] F. Cao, *Geometric curve evolution and image processing*, *Lecture Notes in Mathematics*, vol. 1805, 2003, pp. 1–187.
- [93] F. Gallyas, M. Hsu, G. Buzsaki, Four modified silver methods for thick sections of formaldehyde-fixed mammalian central nervous tissue: 'dark' neurons, perikarya of all neurons, microglial cells and capillaries, *J. Neurosci. Methods* 50 (1993) 159–164.
- [94] N. Otsu, A threshold selection method from gray level histograms, *IEEE Trans. Syst. Man Cybern.* 9 (1979) 62–66.
- [95] J. Roerdink, A. Meijster, The watershed transform: definitions, algorithms and parallelization strategies, *Fundam. Inf.* 41 (2001) 187–228.
- [96] N. Malpica, C.O. de Solorzano, J. Vaquero, A. Santos, I. Vallcorba, J.M. Garcia-Sagredo, F. del Pozo, Applying watershed algorithms to the segmentation of clustered nuclei, *Cytometry* 28 (1997) 289–297.
- [97] J. Feldman, M. Singh, Information along contours and objects, *Psychol. Rev.* 112 (2005) 243–252.
- [98] E. Barenholtz, E. Cohen, J. Feldman, M. Singh, Detection of change in shape: an advantage for concavities, *Cognition* 89 (2003) 1–9.
- [99] M. Bertamini, C. Croucher, The shape of holes, *Cognition* 87 (2003) 33–54.
- [100] J. Norman, F. Phillips, H. Ross, Information concentration along the boundary contours of naturally shaped solid objects, *Perception* 30 (2001) 1285–1294.
- [101] Z. Liu, D. Jacobs, R. Basri, The role of convexity in perceptual completion: beyond good continuation, *Vision Res.* 39 (1999) 4244–4257.
- [102] D. Hoffman, M. Singh, Saliency of visual parts, *Cognition* 63 (1997) 29–78.
- [103] K. Siddiqi, K. Tresness, B. Kimia, Parts of visual form: psychophysical aspects, *Perception* 25 (1996) 399–424.
- [104] H. Resnikoff, *The Illusion of Reality: Topics in Information Science*, Springer, New York, 1985.
- [105] C. Shannon, A mathematical theory of communication, *The Bell System Technical J.* 27 (1948) 379–423.
- [106] K. Thórisson, Simulated perceptual grouping: an application to human-computer interaction, in: *Proceedings of the 16th Annual Conference of Cognitive Science Society*, Atlanta, GA, 1994, pp. 876–881.
- [107] C. Orbert, E. Bengtsson, B. Nordin, Watershed segmentation of binary images using distance transformations, *SPIE J.* 1902 (1992) 159–170.
- [108] H.-C. Liu, M. Srinath, Corner detection from chain-code, *Pattern Recognition* 21 (1990) 51–68.
- [109] J. Russ, *The Image Processing Handbook*, CRC Press, Boca Raton, 2002.
- [110] L. Liu, S. Sclaroff, Region segmentation via deformable model-guided split and merge, *ICCV* 1 (2001) 98–104.
- [111] J. Serra, *Image Analysis and Mathematical Morphology*, vol. 1, Academic Press, London, 1993.
- [112] G. Lin, U. Adiga, K. Olson, J. Guzowski, C. Barnes, B. Roysam, A hybrid 3D watershed algorithm incorporating gradient cues and object models for automatic segmentation of nuclei in confocal image stacks, *Cytometry* 56 (2003) 23–36.
- [113] Q. Yang, B. Parvin, M. Barcellos-Hoff, Localization of saliency through iterative voting, *ICPR*, vol. 1, 2004, pp. 63–66.
- [114] S. Raman, B. Parvin, C. Maxwell, M. Barcellos-Hoff, Geometric approach to segmentation and protein localization in cell cultured assays, in: *ISVC*, 2005, pp. 427–436.
- [115] S. Livens, C. van Roost, P. Scheunders, D. van Dyck, Granulometric segmentation using a gradient convergence map, in: *SCIA97*, 1997, pp. 389–396.
- [116] J. Bigün, G. Granlund, Optimal orientation detection of linear symmetry, in: *Proceeding of ICCV*, 1987, pp. 433–438.

About the Author—OLIVER SCHMITT received his MD from the faculty of medicine of the University of Luebeck in 1991. In his doctoral thesis he analysed neuron distributions of the ageing human brain by first and second order stereology and stochastic geometry. The doctoral thesis was honored by the faculty and the Louise-Eylmann-Foundation. Since 1991 he was responsible for the image analysis core facility of the Medical Faculty of the University of Luebeck. In his habilitation he developed a parallel image analysis system for real time cell recognition in video microscopic imaging. Several cooperations with the Institute of Mathematics and Technical Informatics of the Universities of Luebeck and Rostock concerning multimodal reference free image registration, cell recognition and parallelized image analysis have been established. He is author and coauthor of over 40 published original articles and involved in teaching mathematical image analysis for students of mathematics and informatics. Since 2002 he is a senior lecturer in embryology, molecularbiology, functional histology and macroscopic anatomy at the University of Rostock.